Journal of
Micro/Nanolithography,
MEMS, and MOEMS

Nanolithography.SPIEDigitalLibrary.org

Modeling ellipsometric measurement of three-dimensional structures with rigorous coupled wave analysis and finite element method simulations

Samuel O'Mullane
Nick Keller
Alain C. Diebold

SPIE.

Samuel O'Mullane, Nick Keller, Alain C. Diebold, "Modeling ellipsometric measurement of three-dimensional structures with rigorous coupled wave analysis and finite element method simulations," *J. Micro/Nanolith. MEMS MOEMS* **15**(4), 044003 (2016), doi: 10.1117/1.JMM.15.4.044003.

Modeling ellipsometric measurement of three-dimensional structures with rigorous coupled wave analysis and finite element method simulations

Samuel O'Mullane,[a,*] Nick Keller,[b] and Alain C. Diebold[a]
[a]SUNY Polytechnic Institute, College of Nanoscale Science and Engineering, 257 Fuller Road, Albany, New York 12203, United States
[b]Nanometrics, Inc., 1550 Buckeye Drive, Milpitas, California 95035, United States

Abstract. Using rigorous coupled wave analysis (RCWA) and finite element method (FEM) simulations together, many interesting ellipsometric measurements can be investigated. This work specifically focuses on simulating copper grating structures that are plasmonically active. Looking at near-field images and Mueller matrix spectra, understanding of physical phenomena is possible. A general strategy for combatting convergence difficulties in RCWA simulations is proposed and applied. The example used is a copper cross-grating structure with known slow convergence. Baseline simulations on simple samples are provided for comparison and determination of FEM accuracy. [DOI: 10.1117/1.JMM.15.4.044003]

Keywords: ellipsometry; scatterometry; plasmonics; rigorous coupled wave analysis; finite element method.

Paper 16014P received Feb. 22, 2016; accepted for publication Sep. 27, 2016; published online Oct. 21, 2016.

1 Introduction

1.1 *Ellipsometry and Optical Critical Dimension*

Due to its nondestructive nature and fast data acquisition time, ellipsometry is an ideal optical metrology tool, used extensively throughout semiconductor manufacturing.[1] Fundamentally, ellipsometers measure the change in the polarization state of incoming light due to interaction with a sample's surface.[2] Optical critical dimension (OCD) analysis makes use of this data in conjunction with a structure that closely matches the experimental reality (using SEM, TEM, and so on, information) to model the system.[3] Typically, some regression-based fitting is involved, i.e., structural parameters are varied in order to minimize deviation from the experimental data.[4] When the figure-of-merit (usually mean square error) is minimized, the structural parameters are determined and compared again to other metrology tools for value confirmation, although some variation is expected depending on the method used for comparison.[5]

The most common simulator type for ellipsometry-based OCD tools is rigorous coupled wave analysis (RCWA). As for ellipsometry, RCWA has found favor in industry for its fast computation time and accuracy for typical samples.[6] For more complex samples, RCWA can fail to converge to an appropriate solution.[7] One specific category where RCWA has difficulty is metallic materials which display plasmonic activity.[8] This has been known for 20 years specifically for metallic gratings.[9] The work that follows will address these issues.

1.2 *Motivation*

Although this work will focus on copper-based gratings, the general principles laid out below are applicable to scatterometric targets with resonant behavior. Using electromagnetic field images from finite element method (FEM) simulations in conjunction with Mueller matrix spectra from RCWA simulations allows for a fuller understanding in a phenomenological sense. Put another way, ellipsometry data can be analyzed in terms of near-field phenomena assuming there is some resonance of interest. This could be used to separate resonant phenomena from simple dielectric responses when spectra contain features of unknown origin.

It is well known that RCWA can reproduce surface plasmon resonances (SPR) accurately in terms of spectral location.[10] Modeling the entire ellipsometric spectra for such a sample is considerably more challenging, often overlooked in favor of resonant agreement. Due to the nature of optical modeling in general and RCWA specifically, such resonance-only modeling is bound to produce inaccurate conclusions. Specifically, while basic RCWA simulations produce correct pitch-dependent SPR for metallic gratings, modeling the rest of the structure, e.g., width, thickness of grating, and composition of underlying layers, is ignored. Additionally, the experimental spectral features with physical significance may be absent in RCWA simulations for such structures. For example, copper cross-grating structures produce various easily reproducible surface plasmon features; however, full modeling requires inclusion of localized plasmon features which have different spectral behavior depending on the RCWA simulation accuracy.

1.3 *Plasmonics*

Since the main sample of interest in this work is plasmonically active, a brief background on plasmonics will be presented. Broadly speaking, plasmons describe what happens when electromagnetic fields are confined over subwavelength dimensions. The most familiar plasmon is produced due to the interaction of incoming light with a metallic surface. If this metallic surface is small and structured, the

*Address all correspondence to: Samuel O'Mullane, E-mail: somullane@nanometrics.com

1932-5150/2016/$25.00

plasmon is localized to that small area or volume, hence the term localized plasmon. If the metallic surface can be approximated as flat and continuous over the measured volume, the plasmon is confined to the surface of the metal, hence the term surface plasmon.

Since these two plasmons have different effects on our simulated spectra, they will be separated in this introduction. First, surface plasmons and then localized plasmons will be discussed. Additional detail and discussion is provided with the analysis in the sections that follow.

For analysis purposes, split transverse electric (TE, s) and transverse magnetic (TM, p) incoming light due to different boundary conditions and assume no cross-polarization response. For these modes incident on a planar interface, Maxwell's equations can be written as

(TE polarization)

$$H_x = i\frac{1}{\omega\mu_0}\frac{\partial E_y}{\partial z}, \quad H_z = \frac{\beta}{\omega\mu_0}E_y,$$
$$\frac{\partial^2 E_y}{\partial z^2} + (k_0^2\epsilon - \beta^2)E_y = 0.$$

(TM polarization)

$$E_x = -i\frac{1}{\omega\varepsilon_0\varepsilon}\frac{\partial H_y}{\partial z}, \quad E_z = \frac{-\beta}{\omega\varepsilon_0\varepsilon}H_y,$$
$$\frac{\partial^2 H_y}{\partial z^2} + (k_0^2\epsilon - \beta^2)H_y = 0,$$

where β is the propagation constant and ω is the wave vector of the propagating wave.

For each set of equations above, the first two are the governing equations while the third is the wave equation for those modes. Define $z > 0$ to be dielectric (air) above a metal surface and $z < 0$ to be a semi-infinite slab of metal. While these equations could be solved simultaneously, their solutions have different physical significance. Looking first at the TM equations, the solution is

(TM sol'n, $z > 0$)

$$H_x = i\frac{1}{\omega\mu_0}\frac{\partial E_y}{\partial z}, \quad H_z = \frac{\beta}{\omega\mu_0}E_y,$$
$$\frac{\partial^2 E_y}{\partial z^2} + (k_0^2\epsilon - \beta^2)E_y = 0.$$

(TM sol'n, $z < 0$)

$$E_x = -i\frac{1}{\omega\epsilon_0\epsilon}\frac{\partial H_y}{\partial z}, \quad E_z = \frac{-\beta}{\omega\epsilon_0\epsilon}H_y,$$
$$\frac{\partial^2 H_y}{\partial z^2} + (k_0^2\epsilon - \beta^2)H_y = 0,$$

where subscripts M indicate metal layer quantities and D indicate dielectric layer quantities. If we require $A_D = A_M$ and look at the continuity of the electric fields across the interface, two relations are produced:

$$\frac{k_M}{k_D} = -\frac{\epsilon_M}{\epsilon_D},$$

$$k_i^2 = \beta^2 - k_0^2\epsilon_i,$$

which can further be combined to determine the surface plasmon dispersion relation

$$\beta = k_0\sqrt{\frac{\epsilon_D\epsilon_M}{\epsilon_D + \epsilon_M}}.$$

Consider that the first relation requires the indices of the metal and dielectric permittivity be opposite in sign while the second relation implies that $\beta > k_0$ for plasmonic applications. Consequently, devices must make use of some form of coupling to bridge the gap between the light line and the surface plasmon, either a prism or a nanostructure on the sample surface. The most common nanostructuring is a simple grating due to large scalability and ease of production; the simulations produced for this work are all grating-based.

Surface plasmons require some penetration depth in the metal, e.g., a perfect conductor cannot support surface plasmons while real metals can. Grating geometries are a source of effective penetration depth so that perfect conductors can support surface plasmons as well—these are called spoof or designer plasmons as the plasmonic resonance can be tuned by changing the geometry of the grating. Importantly, this means the spectra produced from plasmonic gratings composed of real metals can be dominated by the spoof plasmons and not the simply derived equation above. Spoof plasmons form a rarely experimentally studied subset of potentially localized plasmon resonances.

Taking the above derivation and attempting to use TE modes instead of TM modes produces the boundary condition $A_M(k_M + k_D) = 0$ due to continuity of the fields at the interface. There is no nontrivial solution to this equation, thus TE modes cannot sustain SPR. Note that both TM and TE modes can support localized (nonpropagating) modes such as those seen in cavity excitations.

Using a simple conservation of momentum argument, it is straightforward to derive the grating coupling equation that is so often used in surface plasmon literature

$$\vec{\beta} = \vec{k}_{\text{in}} + m\vec{k}_p,$$

where k_{in} is the input light wavevector, β is the surface plasmon dispersion derived above, and k_p is the grating wavevector, inversely related to the pitch of the grating. The integer m denotes the order of the SPR, although it is often set to -1, the primary resonance. Considering the limited wavelength region over which this work focuses (due to ellipsometry considerations), only this one order will be visible in spectra. The vector nature of this equation comes into play when the azimuthal angle changes from zero degrees, perpendicular to the grating.

The samples that are of most interest in this work are fully three-dimensional (3-D) and include many more orders of complexity. Instead of plasmons being produced only top-down on flat metal–insulator interfaces, additional coupling can occur through the dielectric in any of the three spatial dimensions. With asymmetrical parameter choices for these three dimensions, each azimuthal angle of measurement and angle of incidence produces different plasmon characteristics.

Localized plasmons, commonly thought of as particle plasmons, occur when isolated subwavelength metal nanostructures are excited into electrical resonance due to the applied electromagnetic field. For particles smaller than 0.1 μm and incident light in the visible or infrared region, the dipole approximation is valid whereby localized plasmons are induced by a resonance in the polarizability of the metal sphere

$$\alpha = 4\pi r^3 \frac{\epsilon_m - \epsilon_d}{\epsilon_m + 2\epsilon_d},$$

where r is the radius of the sphere. This can be generalized for an arbitrarily shaped object and further calculations comprising Mie theory can account for larger sized particles that require electrodynamic considerations. Plasmons of this sort are referred to as Mie plasmons.

Localized plasmonic effects are also present in metal samples which can be used for tunable absorption of light. One such application seen in the literature is a gold grating interspaced with dielectric for tunable absorption in the far-IR.[11] These plasmons are Fabry–Pérot-like cavity modes which are dependent on the entire geometry of the grating structures. This is the basis of our major findings: cavity modes can be used to dramatically increase sensitivity to feature dimensions even for simple copper-dielectric structures.

2 Simulation Methods

As mentioned, the two simulations methods used in this work are RCWA (NanoDiffract, provided by Nanometrics) and FEM (JCMWave). While the RCWA software is well suited to scatterometric measurements, the FEM required additional subroutines to calculate quantities such as Jones and Mueller matrices. For metallic samples specifically and complex samples in general, RCWA can fail to converge, leading to inaccurate modeling of ellipsometric data. The speed with which RCWA computations can be processed is unmatched for these purposes, making it the preferred method, so some check is required for accurate modeling. There are thus three key steps to modeling a sample with the methods to be presented:

1. Ensure FEM accuracy by modeling a simple sample with known RCWA or experimental data.
2. Simulate sample of interest with FEM, produce baseline data.
3. Use baseline data to ensure RCWA convergence for sample of interest, then use RCWA for further calculation.

As will be described, RCWA and FEM are momentum- and real-space numerical simulation methods, respectively. It is clear that agreement between these methods will occur when both are producing accurate, physical results. When this agreement is achieved, simulations can proceed with RCWA as normal, only checking FEM agreement as necessary. Note that step 1 refers to the accuracy of the FEM simulator, not the accuracy of the simple sample mentioned. It is assumed that a simple sample will be easily modeled and confirmed correct with complementary techniques, e.g., measurement and verification of a thin film sample.

2.1 *Rigorous Coupled Wave Analysis*

Derived from Fourier-transformed Maxwell's equations, RCWA is a momentum-space method that reduces optical interactions to a $2N + 1$ eigenvalue search for each polarization of interest (usually both p- and s-polarizations). To get to this point, the full Fourier series has been truncated at N terms. The eigenequation can be written in the standard form $A\xi = b$ where A is a (4×4) matrix describing the interaction, ξ is the (4)-vector containing reflection and transmission coefficients, and b essentially contains the boundary conditions. Note that the elements of A are $(2N + 1 \times 2N + 1)$ matrices; this explains the search size mentioned earlier. The computational domain here is defined in terms of a spatially varying dielectric function, taking care to Fourier transform to an equivalent representation if approximations are used. This is to avoid Gibbs phenomena where real space representations of high-dielectric-contrast structures (such as straight sidewall rectangular gratings) cause numerical instability in the resulting RCWA simulations.[12]

Crucial to the discussion in the results section is the concept of convergence. When the Fourier series is truncated, or approximated, some numerical error is introduced. If this error becomes large enough, the approximation produced by RCWA is no longer accurate, thus the simulation has failed to converge to the solution value. For metallic materials, this problem is prevalent and care must be taken to ensure convergence is achieved.

2.2 *Finite Element Method*

For any FEM simulation, the computational domain is divided into many triangular and rectangular elements (composing a mesh) with more elements at key locations such as at an interface or where some feature of interest is located. The partial differential equations (here Maxwell's equations) are then discretized over the mesh and numerically analyzed. The solution set is approximated by polynomial vector fields. As such there is a residual-based error estimation that can be used for further mesh refinement.

For this work, the FEM has been set up specifically to model the ellipsometric measurement process. In addition to using Maxwell's equations to describe the input fields and boundary conditions, ellipsometric input and exit angles were used. Additionally, azimuthal rotation was included for simulation flexibility. In the postprocessing portion of the FEM, output fields were converted into Jones and Mueller matrix quantities in order to analyze optical interactions simply and in a similar manner to standard RCWA practice.

2.3 *Comparison for Simple Samples*

By convention, the Mueller matrix element M_{12} is used for most simulation representations since it is simply related to the amplitude change ψ

$$M_{12} = \frac{1 - \tan^2(\psi_{pp}) - \tan^2(\psi_{ps}) - \tan^2(\psi_{sp})}{1 + \tan^2(\psi_{pp}) + \tan^2(\psi_{ps}) + \tan^2(\psi_{sp})},$$

where for the ψ terms the first subscript indicates the polarization of the incoming light while the second subscript indicates the polarization of the reflected light. For nonconical diffraction modes, this reduces to a simple sinusoidal dependence on the amplitude change.

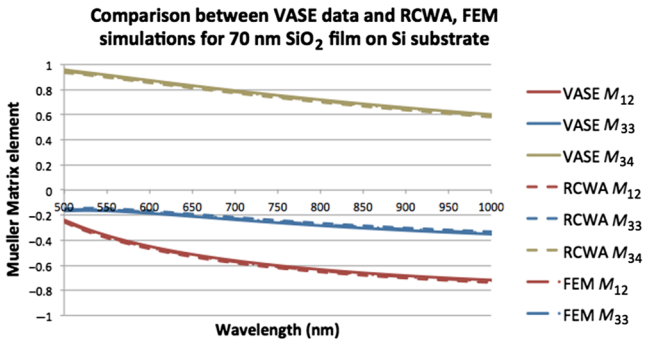

Fig. 1 Comparison between VASE data and RCWA and FEM simulations for a 70-nm SiO_2 film on a Si substrate. Nominal thickness used for simulation explains offset among the three sources.

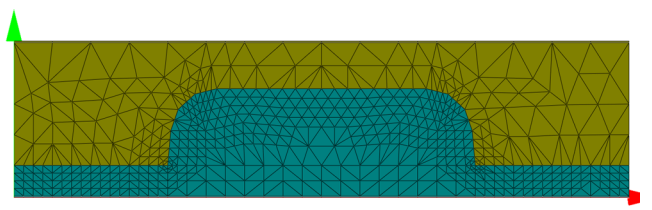

Fig. 2 Mesh produced by FEM simulator for rounded silicon lines on silicon substrate (teal) with air surroundings (dark yellow). Note smaller mesh elements at interfaces and where there are sharp changes in the dielectric function.

To confirm that the FEM is producing experimentally verifiable results, simple thin film simulations were performed such as the one presented in Fig. 1. For a 70-nm SiO_2 thin film on a Si substrate, both simulation methods line up closely with the variable angle spectroscopic ellipsometry (VASE) data. The nominal thickness value was used for both simulation methods, thus explaining the slight offset between data sets.

Figure 2 shows an example sample, a simple rounded silicon line on a silicon substrate with air surroundings. Note that this is a periodic structure: the representation shown is for one unit cell of an infinite array in the x-direction (left to right) and y-direction (into and out of the page), with nonperiodicity in the remaining z-direction. Since RCWA requires this periodicity, all FEM simulations shown will likewise maintain these restrictions for consistency and comparison. While largely featureless (and thus omitted), these simulations are useful for tuning the mesh of FEM and harmonics of RCWA.

Figure 3 shows a comparison plot between RCWA (lines) and FEM (symbols) simulations for a simple two-dimensional (2-D) copper grating with a pitch of 200 nm and width (critical dimension, CD) of 100 nm. Good agreement is maintained for the majority of the spectra with some error present around 1025 nm. This is likely due to the FEM step size which was set at 25 nm for this data set. As such, sharp features would not necessarily be sampled properly leading to apparent disagreement even when the two methods agree.

In addition to the samples mentioned above, various thin film and anisotropic grating measurements with known experimental data were reproduced with the FEM, including conical diffraction effects at nontrivial azimuthal angles. This demonstrates that the FEM is functioning properly and can be used to provide the baseline data for more complex samples to check RCWA convergence.

2.4 *Sample of Interest Description*

As mentioned in the introduction, certain samples are particularly difficult to model in RCWA. The main focus of this work is modeling copper cross-gratings that display localized plasmon spectral features. These are shown schematically in Fig. 4, with standard parameter choices shown in Table 1. Note that these are reference values, the phenomena seen occur for a broad range of choices, sometimes with improved, desired results, e.g., sensitivity to changes in CD increase as the CD decreases. For prospective users, these structures will greatly enhance the sensitivity of key parameters used in optical metrology. Specifically, the presented results show marked improvement in metallic line width sensitivity with likely additional sensitivity to potential rounding or shape deformation. As such, this structure would primarily be a characterization-enhancement structure, although there are reasonable extensions to tool calibration for improved matching based on a characteristic plasmonic feature. Other characteristics such as electrical properties are beyond the scope of this work.

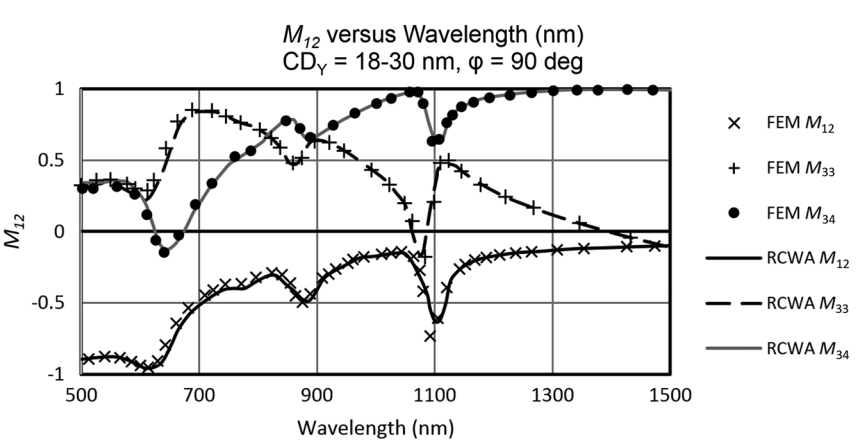

Fig. 3 Comparison plot between RCWA and FEM for 2D Cu gratings on silicon substrate. $P = 200$ nm, CD = 100 nm, AOI = 75 deg, azimuthal angle = 0 deg. Additional FEM data needed for closer match near 1025 nm feature.

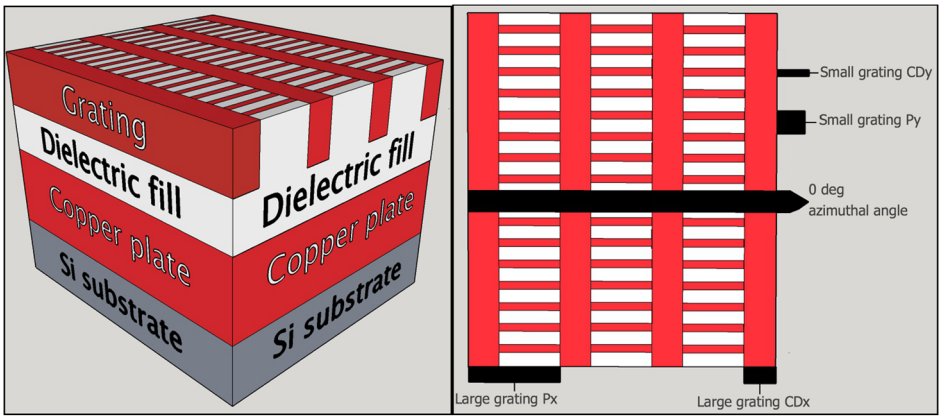

Fig. 4 Schematics of cross-grating test structure. (a) 3-D view of cross-grating with labeled stack: Si substrate–Cu plate–dielectric fill—top copper grating layer. (b) Top-down view with labeled azimuthal angle convention and relevant simulation parameters *P*, CD.

Table 1 Reference parameters of cross-grating if not explicitly stated.

CD_X (width of x-grating)	0.12 μm
CD_Y (width of y-grating)	30 nm
P_X (pitch of x-grating)	0.6 μm
P_Y (pitch of y-grating)	120 nm
T_1 (thickness of dielectric)	50 nm
T_2 (thickness of grating)	20 nm
T_P (thickness of copper plate)	50 nm
AOI (angle of incidence)	65 deg

3 Results and Discussion

In Sec. 2.3, agreement was assured between FEM and RCWA for simple structures. Now the FEM can be used to analyze known and unknown spectral features in terms of magnetic near-field images. From a simple analysis of Maxwell's equations with boundary conditions appropriate for s- and p-polarized light, it is trivial to see that only p-polarized light can couple with the grating to produce surface plasmons. Since the wave equation for p-polarized light is

$$\frac{\partial^2 H_y}{\partial z^2} + (k_0^2\epsilon - \beta^2)H_y = 0,$$

it is standard practice to show field images in terms of the magnetic field. This is also a practical consideration: electric field resonances appear as sharp point-like features at interfaces while magnetic field resonances are broad and intuitive.

3.1 *Three-Dimensional Plasmonic Grating*

Before turning to full 3-D cross-gratings, it is informative to analyze simple 2-D copper gratings. These are pictured both schematically and in FEM mesh form in Fig. 5. For the given parameters listed, Mueller matrix spectra for the elements M_{12}, M_{33}, and M_{34} are shown in Fig. 6. Each of these elements has one nondielectric-based feature: a maximum or minimum when the input light has a wavelength of 950 nm. The plasmonic nature of this feature, as well as the confidence that it is the only feature of interest, is determined using magnetic field images as described below.

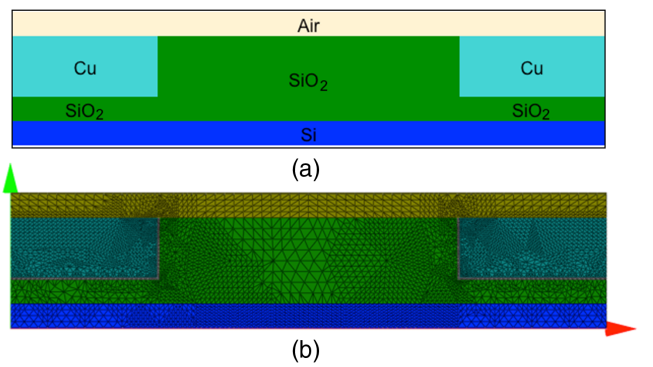

Fig. 5 (a) Schematic of simple half-space Cu grating structure and (b) 2-D FEM mesh of same structure.

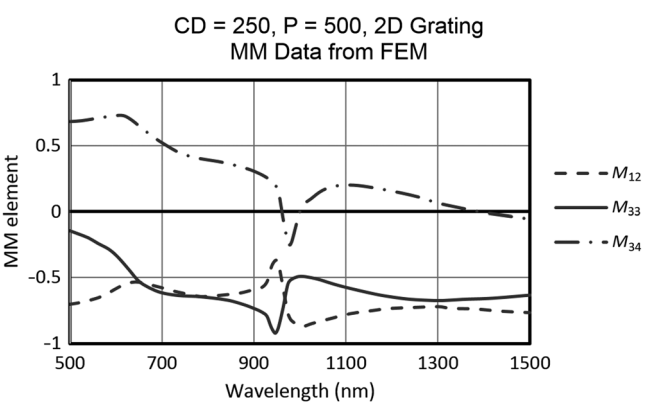

Fig. 6 M_{12}, M_{33}, M_{34} versus the wavelength of light for simple half-pitch copper grating, $\varphi = 0$. Plasmonic effect at 950 nm predicted by grating equation, 600 nm variation due to copper-dielectric function.

Fig. 7 H field for simple half-pitch copper grating, $\varphi = 0$, $\lambda = 600$ nm. Dark blue $H = 0$ μA/m, red (max, not seen) $H = 50$ μA/m. White rectangles outline the area of copper, the remaining structure is dielectric fill apart from above the copper where air is present.

Fig. 8 H field for simple half-pitch copper grating, $\varphi = 0$, $\lambda = 950$ nm. Dark blue $H = 0$ μA/m, red $H = 50$ μA/m. SPR above Cu.

Although field images were produced for the entirety of the spectra in Fig. 6, only two are shown to explain the given phenomena. In Fig. 7, the standard dielectric response is seen for a given input wavelength of 600 nm. This is characteristic of the majority of the simulated spectra. Since there are no clear features, it can be assumed that this is the baseline for a copper grating when no coupling is present.

Compare this with Fig. 8 where there are extremely intense pockets of magnetic field located above the copper portion of the grating. This is exactly what one would expect to see for SPR when coupling to a metallic grating. As such, spectral features for copper gratings between 800 and 2000 nm such as the one seen in Fig. 5 indicate some form of plasmonic resonance. Determination of character requires magnetic field image simulations.

When a copper plate is added in between the top copper grating and the dielectric fill, localized plasmonic resonances occur due to a coupling between the two metallic layers. This has been explained as a Fabry–Perot-like resonance, detailed in Ref. 13. Confirmation of this effect is seen in Figs. 9 and 10, showing a higher order and fundamental localized plasmon resonance, respectively.

These two effects, surface and localized plasmons, will be visible in the full 3-D copper cross-grating and determination of their character has been determined using images as shown above. Only Mueller matrix spectra will be shown with resonance character indicated as appropriate.

3.2 *Three-Dimensional Plasmonic Cross-Grating*

For the full cross-grating structure, further analysis of Mueller matrix spectra can be achieved by looking at the p- and s-components reflectance values. Begin with the M_{12} spectra in Fig. 11 with one surface plasmon at 700 nm, two localized plasmon minima, and two localized plasmon maxima.

Figure 12 contains the p- and s-polarized components of the reflectance, showing that minima in R_P induce maxima in M_{12} while minima in R_S produce minima in M_{12}. This is shown for a wide range of smaller grating widths (CD_Y), showing that the localized minima are extraordinarily dependent on the CD of the structure. In previous work,[14] the location of these minima was thought to be dependent on the fill factor (ratio of the grating to unit cell area) which produces higher order resonances with increasing CD. As seen in Figs. 13 and 14, the true behavior is a trend toward a single minima value with increasing CD. This is a real, physical difference that would have been overlooked without careful FEM analysis.

With a thorough baseline and understanding as detailed above, convergence of RCWA can finally be tested. Example spectra are shown in Fig. 15, showing very good agreement between two largely incompatible methods. Note that the FEM step size in the right figure is again too broad to claim significant disagreement between the methods. This is a vast improvement over previous publications which settled for reproducing only SPR, ignoring the physically significant ambient spectra.

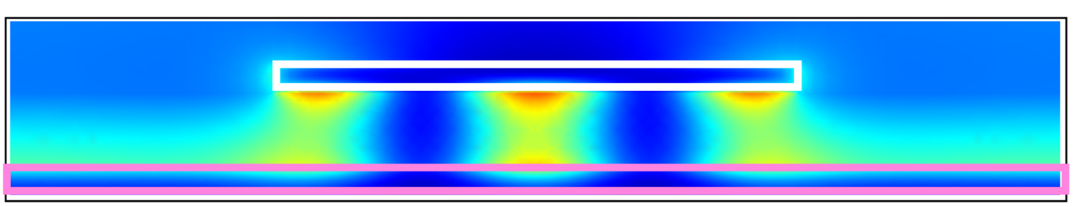

Fig. 9 H field for cross-grating structure, $\varphi = 0$, $\lambda = 700$ nm. Dark blue $H = 0$ μA/m, red $H = 50$ μA/m. Localized plasmon activity in between copper grating (white outlined rectangle) and copper plate (pink outlined rectangle, substrate). Dielectric fill between copper is SiO_2.

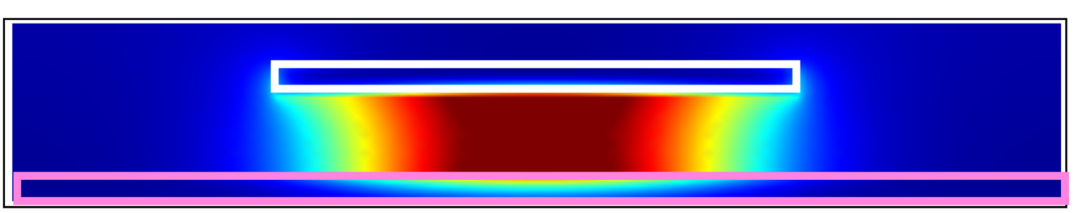

Fig. 10 H field for cross-grating structure, $\varphi = 0$, $\lambda = 1450$ nm. Dark blue $H = 0$ μA/m, red $H = 50$ μA/m. Localized plasmon activity in between copper grating and copper plate.

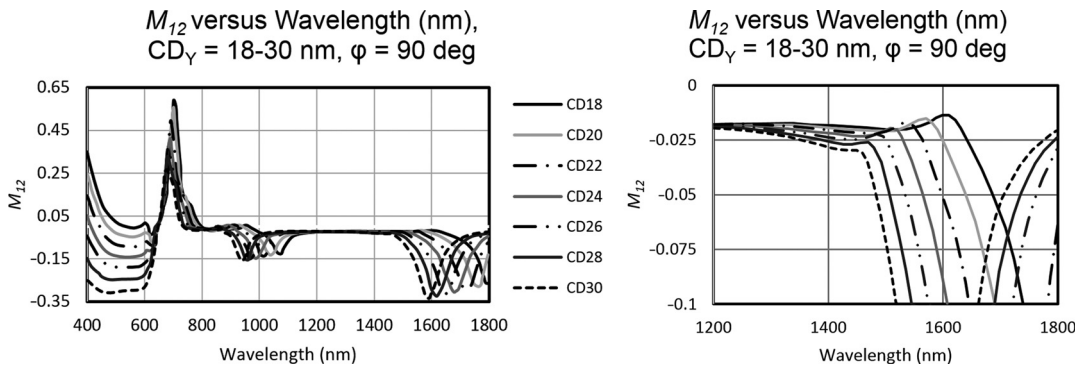

Fig. 11 M_{12} versus the wavelength of light for a variety of CD values for the small copper lines in a cross-grating. $\varphi = 90$. (a) Entire spectra and (b) zoomed in on maxima, for various widths of the smaller grating (CD). Two clear orders of localized plasmon seen. Remaining structural parameter choices can be found in Table 1.

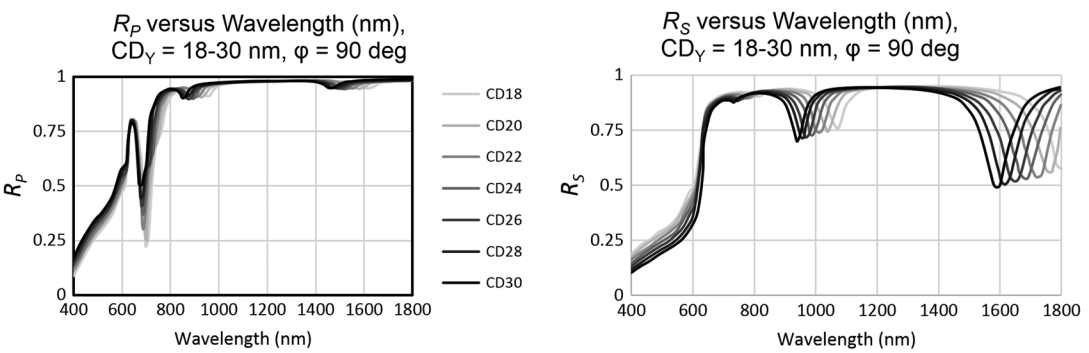

Fig. 12 The p-polarized reflectance R_P and s-polarized reflectance R_S versus the wavelength of light for a variety of CD values for the small copper lines in a cross-grating. $\varphi = 90$, (a) R_P and (b) R_S for various widths of the smaller grating (CD). Two clear orders of localized plasmon seen. Remaining structural parameter choices can be found in Table 1.

Comparisons between RCWA and FEM simulations can be made for all parameter variations of a given structure. For example, variation of the height of the top copper grating, T_2, is analyzed in Fig. 16 using both methods. It is clear that some step size and model refinement is needed for exact agreement. Improvement can be achieved if the cost limitations of RCWA and time limitations of FEM are overcome. Specifically, these RCWA simulations were produced using Nanometrics' new Chorus computation engine with cloud computing capabilities to assure convergence and decrease time of computation. As for the FEM, a single wavelength simulation takes on the order of 5 min to complete and an ellipsometric spectra contains between 50 and 200 wavelengths, i.e., 4 h of computation time. If lack of convergence is an issue of interest, overcoming one of these limitations would be sufficient to verify solution applicability.

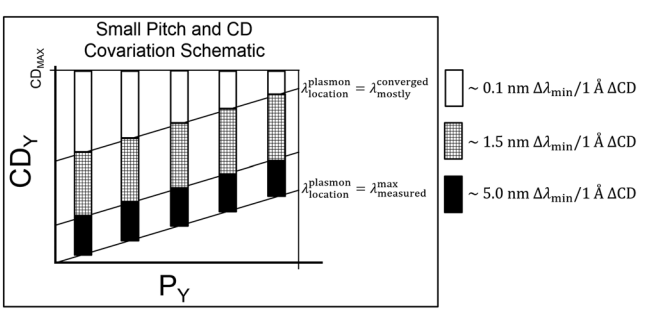

Fig. 13 Covariation schematic detailing plasmon minima location with respect to CD and pitch (of the smaller grating in the cross-grating) with sensitivity scale listed on right-hand side. These are example values calculated for approximately median minima. $\lambda^{plasmon}_{location}$ is where the localized minima appears in an M_{12} spectra, $\lambda^{max}_{measured}$ is the limit of the tool or simulator, $\lambda^{mostly}_{converged}$ is the point where changes in CD have little effect, comparable to standard copper line array sensitivity. See Fig. 12 for example spectra.

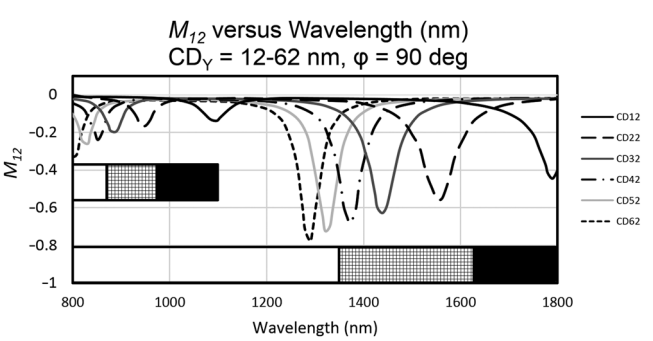

Fig. 14 Large-scale CD variation of smaller grating, demonstrating convergence toward single minima for larger CD values. For example, significantly more sensitivity to change in CD for 12 to 22 nm transition than 22 to 32 nm transition. Large blocks at bottom refer to primary order, smaller blocks near −0.4 M_{12} are for second-order localized plasmons, key can be found in Fig. 13. For the simulations shown, $\lambda^{max}_{measured} = 1800$ nm, $\lambda^{mostly}_{converged} = 1375$ nm.

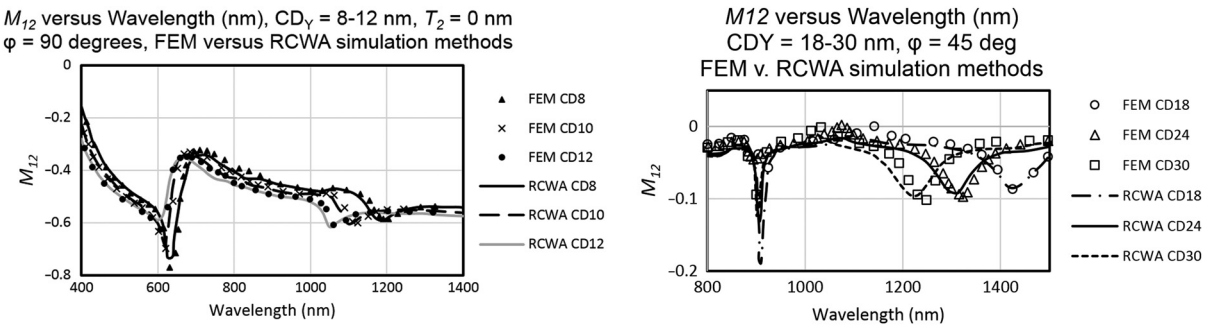

Fig. 15 Mueller matrix element M_{12} versus the wavelength of light for varying CD_Y simulated by both FEM and RCWA. Good agreement found for location of plasmonic effects.

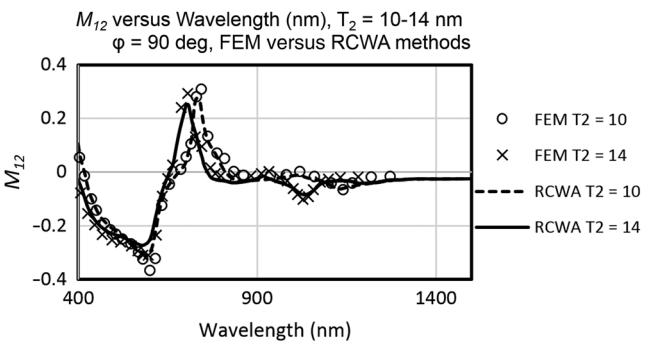

Fig. 16 Mueller matrix element M_{12} versus the wavelength of light for varying T_2 simulated by both FEM and RCWA. Good agreement found for location of plasmonic effects.

4 Conclusion

Using FEM calculations as a source of comparison, RCWA simulations can be tested and adjusted for convergence regardless of previous computational difficulties. Additionally, analysis of Mueller matrix spectra in terms of magnetic field images has been presented, offering a path toward phenomenological optical metrology. Due to agreement between real and momentum-space methods, experimental confirmation is expected in the near future when samples are prepared. Quantification of results will follow once regression is implemented into the FEM simulations and a sample is prepared as described.

Acknowledgments

Thanks to Nanometrics for funding and providing the RCWA software NanoDiffract, as well as access to the new RCWA engine and cloud computation services that proved to be crucial to achieving convergence. Additional thanks to JCMWave for FEM support from start to finish.

References

1. A. C. Diebold, *Handbook of Silicon Semiconductor Metrology*, Marcel Dekker, New York (2001).
2. H. Fujiwara, *Spectroscopic Ellipsometry: Principles and Applications*, John Wiley & Sons, Chichester, England (2007).
3. T. Novikova et al., "Application of Mueller polarimetry in conical diffraction for critical dimension measurements in microelectronics," *Appl. Opt.* **45**(16), 3688 (2006).
4. W. Yang et al., "Line-profile and critical-dimension monitoring using a normal incidence optical CD metrology," *IEEE Trans. Semicond. Manuf.* **17**(4), 564–572 (2004).
5. D. Dixit et al., "Metrology for directed self-assembly block lithography using optical scatterometry," *Proc. SPIE* **9050**, 90500N (2014).
6. R. J. Hoobler and E. Apak, "Optical critical dimension (OCD) measurements for profile monitoring and control: applications for mask inspection and fabrication," *Proc. SPIE* **5256**, 638 (2003).
7. Y. Ma et al., "Estimation of the convergence order of rigorous coupled-wave analysis for OCD metrology," in *Seventh Int. Symp. on Precision Engineering Measurements and Instrumentation* (2011).
8. L. Li and C. W. Haggans, "Convergence of the coupled-wave method for metallic lamellar diffraction gratings," *J. Opt. Soc. Am. A* **10**(6), 1184 (1993).
9. S. Peng and G. M. Morris, "Efficient implementation of rigorous coupled-wave analysis for surface-relief gratings," *J. Opt. Soc. Am. A* **12**(5), 1087 (1995).
10. M. Bergmair, *Spectroscopic Ellipsometry on Metallic Gratings and the Energy Density in Absorbing Media*, Trauner Verlag, Linz (2012).
11. Y. Ho, G. Lerondel, and J. Delaunay, "Plasmonic hybrid cavity-channel structure for tunable narrow-band optical absorption," *IEEE Photonics Technol. Lett.* **26**(19), 1979–1982 (2014).
12. M. Weismann, D. F. G. Gallagher, and N. C. Panoiu, "Accurate near-field calculation in the rigorous coupled-wave analysis method," *J. Opt.* **17**(12), 125612 (2015).
13. S. O'Mullane, "Plasmonic enhancement of the ellipsometric measurement of thin metal lines," Thesis, SUNY at Albany (2015).
14. S. O'Mullane et al., "Enhancing one dimensional sensitivity with plasmonic coupling," *Opt. Express* **22**(21), 26246 (2014).

Samuel O'Mullane received his doctorate in nanoscience from State University of New York at Albany in 2015. His dissertation was titled "Plasmonic Enhancement of the Ellipsometric Measurement of Thin Metal Lines." In 2016, he joined in a nanometrics as an applications scientist.

Nick Keller received his BSEE from the University of California, Santa Barbara, in 2007. He joined Nanometrics in 2007 as an applications engineer.

Alain C. Diebold is a interim Dean College of Nanoscale Sciences at SUNY Polytechnic Institute. He is a Empire Innovation Professor of Nanoscale Science and Executive Director, Center for Nanoscale Metrology at SUNY Poly. He maintains an active research effort in the area of the optical properties of nanoscale materials and measurements of nanoscale structures. He is a fellow of both the American Vacuum Society and SPIE. He is an associate editor for *IEEE's Transactions on Semiconductor Manufacturing*.